Unique Domain Structure of Two-Dimensional α-Mo$_2$C Superconducting Crystals

Zhibo Liu,[†] Chuan Xu,[†] Ning Kang,[‡] Libin Wang,[‡] Yixiao Jiang,[†] Jiao Du,[‡] Ying Liu,[†] Xiu-Liang Ma,[*,†] Hui-Ming Cheng,[†] and Wencai Ren[*,†]

[†]Shenyang National Laboratory for Materials Science, Institute of Metal Research, Chinese Academy of Sciences, Shenyang 110016, P. R. China

[‡]Key Laboratory for the Physics and Chemistry of Nanodevices and Department of Electronics, Peking University, Beijing 100871, P. R. China

S *Supporting Information*
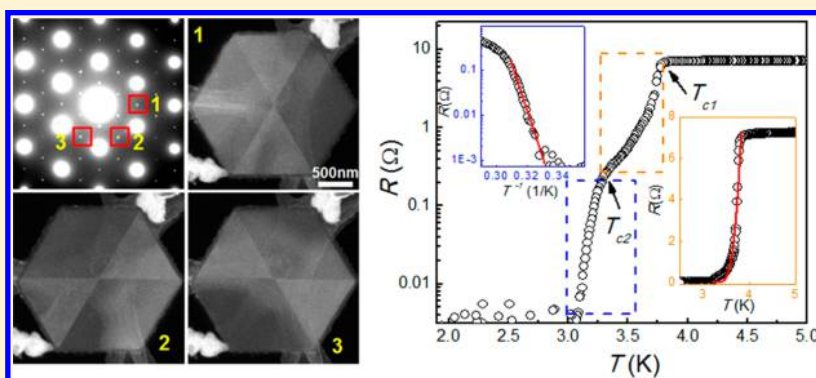
ABSTRACT: The properties of two-dimensional (2D) materials such as graphene and monolayer transition metal dichalcogenides are strongly influenced by domain boundaries. Ultrathin transition metal carbides are a class of newly emerging 2D materials that are superconducting and have many potential applications such as in electrochemical energy storage, catalysis, and thermoelectric energy conversion. However, little is known about their domain structure and the influence of domain boundaries on their properties. Here we use atomic-resolution scanning transmission electron microscopy combined with large-scale diffraction-filtered imaging to study the microstructure of chemical vapor deposited high-quality 2D α-Mo$_2$C superconducting crystals of different regular shapes including triangles, rectangles, hexagons, octagons, nonagons, and dodecagons. The Mo atom sublattice in all these crystals has a uniform hexagonal closely packed arrangement without any boundaries. However, except for rectangular and octagonal crystals, the C atom sublattices are composed of three or six domains with rotational-symmetry and well-defined line-shaped domain boundaries because of the presence of three equivalent off-center directions of interstitial carbon atoms in Mo octahedra. We found that there is very small lattice shear strain across the domain boundary. In contrast to the single sharp transition observed in single-domain crystals, transport studies across domain boundaries show a broad resistive superconducting transition with two distinct transition processes due to the formation of localized phase slip events within the boundaries, indicating a significant influence of the boundary on 2D superconductivity. These findings provide new understandings on not only the microstructure of 2D transition metal carbides but also the intrinsic influence of domain boundaries on 2D superconductivity.

KEYWORDS: 2D crystals, α-Mo$_2$C, domain boundary, superconductivity

Two-dimensional (2D) materials, such as graphene and monolayer hexagonal boron nitride and transition metal dichalcogenides, have attracted increasing interest because of their many unique physical and chemical properties that are different from their bulk counterparts.[1−4] Chemical vapor deposition (CVD) has been widely used to grow high-quality 2D materials over a large area,[5−11] which show promising applications in electronics and optoelectronics. However, recent studies have shown that CVD-grown large-area 2D materials are composed of many domains,[5−9] and the domain boundaries have an unusual influence on properties such as carrier mobility, electrical conductivity, mechanical strength, thermal conductivity, and photoluminescence.[5−9]

Two-dimensional superconductivity has been one of the most active topics in condensed matter physics for decades. Similar to other 2D materials, a domain boundary might have a significant effect on the 2D superconductivity. However, most of the 2D superconductors studied so far are either unstable or
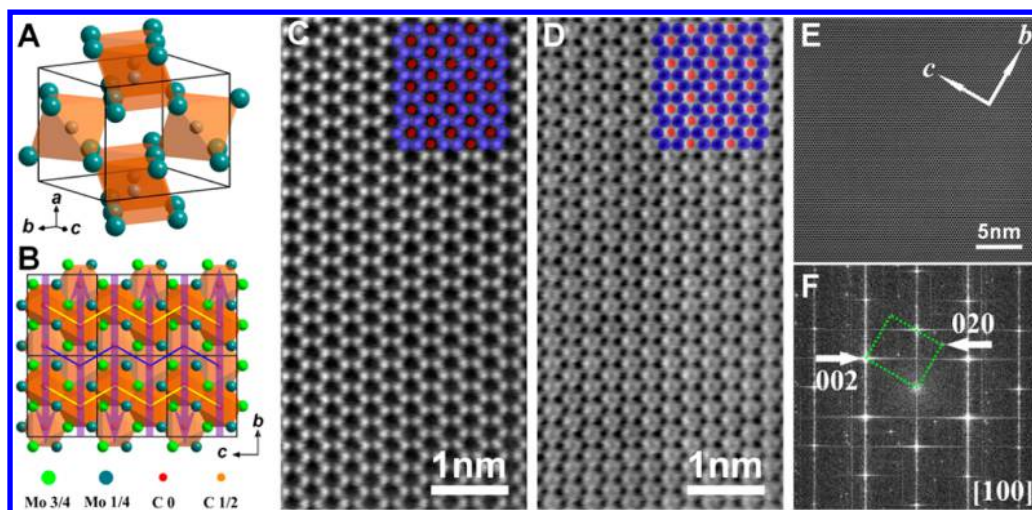
Figure 1. Crystalline structure of 2D α-Mo$_2$C crystals. (A) Atomic model of an unit cell of α-Mo$_2$C crystal. (B) Atomic model of an α-Mo$_2$C crystal projected in the [100] direction. The purple arrows show the off-center directions of carbon atoms in Mo octahedra. Yellow and blue lines show the zigzag configuration of carbon atoms in each layer. (C,D) Atomic-resolution HAADF-STEM image (C) and BF-STEM image (D) of an ultrathin 2D α-Mo$_2$C crystal with superimposed atomic models shown in the top-right insets (blue solid circles represent Mo atoms, and red solid circles represent carbon atoms). (E,F) Large-area HAADF-HRSTEM image (E) and the corresponding FFT pattern (F) of a 2D α-Mo$_2$C crystal.

disordered in addition to containing domain boundaries.[12,13] Ultrathin transition metal carbides (TMCs) are a class of newly emerging 2D materials that are superconducting and have many intriguing applications.[14−17] Recently, a series of large-size high-quality 2D TMC crystals (α-Mo$_2$C, WC, and TaC) have been fabricated by CVD at a temperature above the melting point of Cu, using a bilayer of Cu foil sitting on top of another transition metal foil as the growth substrate, and the ultrathin α-Mo$_2$C crystals produced have been confirmed to be a stable clean 2D superconductor.[14] Such materials open up the possibility of revealing the intrinsic influence of domain boundaries on the 2D superconductivity; however, their domain structure is not clear.

Here we used atomic-resolution scanning transmission electron microscopy (STEM) combined with large-scale diffraction-filtered imaging to investigate the microstructure of CVD-grown high-quality 2D α-Mo$_2$C superconducting crystals. The crystals were prepared as reported previously[14] and have different regular shapes including triangles, rectangles, hexagons, octagons, nonagons, and dodecagons (Supplementary Figure S1). The Mo atom sublattice in all these shaped crystals has a uniform hexagonal closely packed (HCP) arrangement without any boundaries. However, except for rectangular and octagonal crystals, the C atom sublattices have three or six domains with rotational-symmetry and well-defined line-shaped domain boundaries. We found that there is a relatively small lattice shear strain across the domain boundary, but the boundary has a significant influence on the super-conductivity, resulting in a broad resistive superconducting transition with two distinct transition processes due to the formation of localized phase slip events in the boundaries.

As shown in our previous work,[14] a CVD-grown 2D α-Mo$_2$C crystal has an orthorhombic structure and is composed of HCP Mo atoms with interstitial carbon atoms located in half the octahedra[18] (Figure 1A,B). In order to further understand the atomic structure of the 2D α-Mo$_2$C crystal, we performed first-principles calculations based on previously reported neutron diffraction experimental data.[18] The results show that the interstitial carbon atoms in the octahedra are moved slightly off-

center in the **b**-direction of the α-Mo$_2$C lattice (Figure 1B), forming a zigzag configuration along the **c**-direction, which consequently leads to a slight distortion of the Mo sublattice along the **b**-direction (Table S1 and Figure S2). Moreover, there are three equivalent zigzag configurations of carbon atoms associated with the same HCP Mo atom sublattice (Figure S3).

Due to the 2D characteristic of ultrathin α-Mo$_2$C crystals, it is easy to acquire an atomic-resolution image along its [100] zone axis. We should point out that carbon atoms have been rarely, if ever, seen in TMCs by TEM due to their low electron scattering ability compared with heavy metal atoms and the ubiquitous organic contamination that exists in a TEM. The advanced aberration-corrected STEM and our high-quality clean 2D α-Mo$_2$C crystals make it possible to study the structural behavior of both heavy and light elements, i.e., Mo and carbon, in TMCs. Figure 1C shows a high angle angular dark field (HAADF)-STEM image of a 2D α-Mo$_2$C crystal, which is also called a Z-contrast image (the intensity of atoms is approximately proportional to the square of their atomic number, ~Z^2). Consistent with the atomic model shown in Figure 1B, the Mo atoms are arranged with a HCP configuration, showing a graphene-like honeycomb lattice in the [100] projected direction. Because carbon is a much lighter element than Mo, the Z-contrast image cannot give the carbon atom positions. Therefore, we acquired a bright field (BF)-STEM image along the same zone axis to visualize the carbon atom positions (Figure 1D) since the BF-STEM image is sensitive to both light and heavy elements. It can be clearly seen that the carbon atoms are located near the centers of the Mo hexagonal lattice without defects being observed.

Even though the carbon atoms can be seen in BF-STEM images, we could not determine their exact off-center directions because their displacement is too small to be seen by the naked eye. Fortunately, as discussed above, because of the octahedron off-center zigzag configuration of carbon atoms in the α-Mo$_2$C lattice, the sublattice of Mo atoms slightly deviates from the hexagonal configuration into an orthorhombic configuration (Figure S4). Therefore, we can obtain this structural information from reciprocal space by fast Fourier trans-

formation (FFT) analysis. In order to obtain a clear FFT pattern, we acquired a large-area HAADF-HRSTEM image (Figure 1E). As shown in Figure 1F, the corresponding FFT clearly shows a characteristic orthorhombic pattern of the 2D α-Mo$_2$C crystal, which shows the off-center displacement of carbon atoms in the Mo octahedra to be in the reciprocal space vector [020]* direction. Note that this off-center deviation is in the real space **b**-direction, which is consistent with the structural model shown in Figure 1B.

In some ferroelectric materials, the centroids of positive and negative ions are not coincident, so they usually form domains with different orientations, called displacement-type ferroelectric domains.[19,20] The existence of such domains has a strong influence on the physical properties and applications of ferroelectric materials.[21] Similar to these ferroelectric materials, carbon atom positions deviate from the center of the Mo octahedra to form a zigzag configuration, and there are three equivalent configurations in the same Mo atom sublattice. Therefore, if these equivalent zigzag configurations of interstitial carbon atoms exist simultaneously in the same Mo atom sublattice, topological α-Mo$_2$C domains could form.

Selected area electron diffraction (SAED) is an efficient method to identify the crystallographic orientation of crystals, and we therefore used it to study the structure of 2D α-Mo$_2$C crystals with different shapes. Figure 2A shows a TEM image of a hexagonal 2D α-Mo$_2$C crystal. We carried out SAED measurements on areas ①–⑦ indicated in Figure 2A, and the SAED patterns obtained are shown in Figure 2B ①–⑦. It is interesting to find that the SAED patterns of areas ①–⑥ are the same, but the corresponding c*-axis orientations of adjacent areas are rotated by 60°. The SAED pattern of area ⑦ is a superimposition of those of areas ①–⑥ and has pseudo-6-fold symmetry. More importantly, the principal diffraction patterns of Mo sublattices from areas ①–⑥ overlap (e.g., big and bright spots shown in Figure 2B ⑦), indicating that the HCP Mo atom sublattices remain in the same orientation across the whole sheet. For a crystallographic orthorhombic structure, the lattice c-direction of real space is parallel to the c*-direction of reciprocal space. Therefore, the octahedron off-center zigzag configurations of carbon atoms in the six areas are different with a rotation of 60° between each other. This is consistent with the theoretically predicted results discussed above and is responsible for the different crystallographic orientations of different areas observed here. Moreover, the zigzag configuration direction (c-direction) of carbon atoms in each area is perpendicular to the outer edge of the area.

Dark-field TEM (DF-TEM) is a diffraction-sensitive imaging technique, which has recently been widely used to identify the grains of various 2D materials. Here we used DF-TEM to further study the structure of hexagonal α-Mo$_2$C crystals. We selected the (020) ED spots for each domain to obtain the corresponding dark field images (Figure 2C–E). It can be seen that the crystal is composed of six triangular domains, and the difference in the crystallographic orientations of adjacent domains is always 60°, forming domains with 6-fold rotational-symmetry. More interestingly, each domain boundary crosses one vertex and the centroid of the hexagon in a sharp straight line. This is the reason why the ED pattern of area ⑦ is a superimposition of those of areas ①–⑥. Figure 2F is a diagram of the atomic structure of the crystal based on the above SAED and DF-TEM analyses, clearly showing that the hexagonal crystal is indeed a superstructure containing many domains.
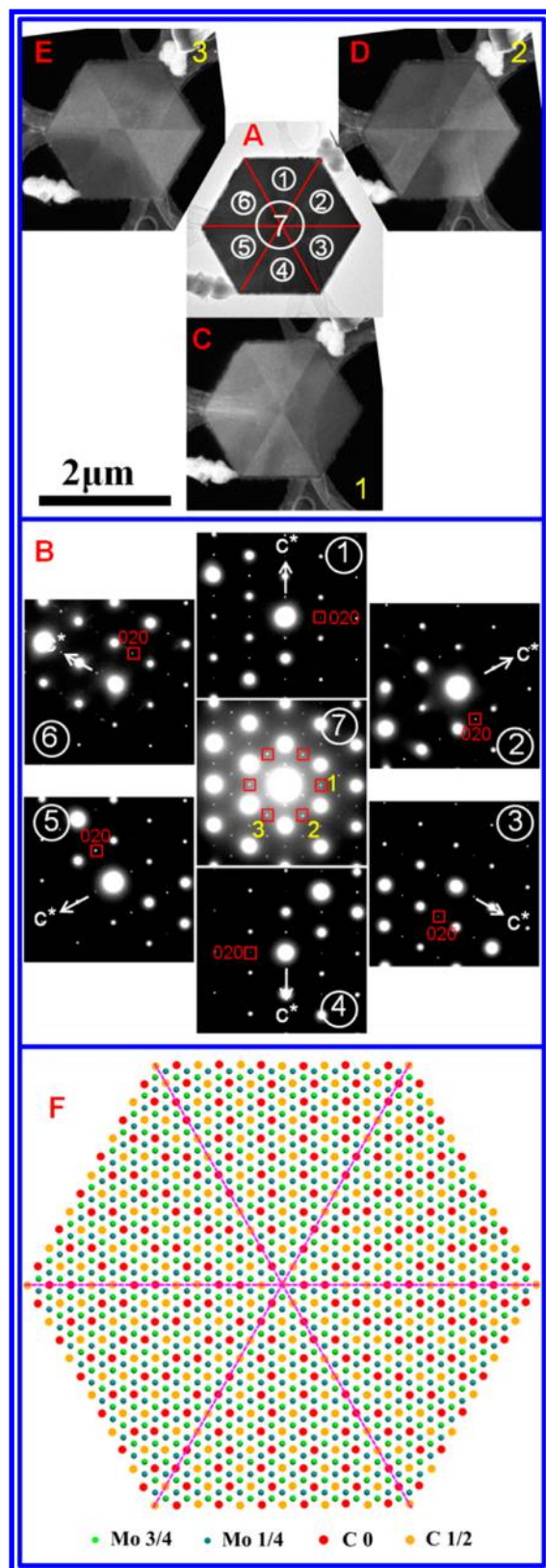
Figure 2. Domains with rotational-symmetry in a hexagonal 2D α-Mo$_2$C crystal. (A) BF-TEM image. (B) ED patterns taken from ①–⑦ areas in (A). Domain-related (020) ED spots are indicated by red boxes. (C–E) DF-TEM images obtained by selecting the ED spots indicated by yellow numbers 1–3 in (B), showing domains with 6-fold rotational-symmetry. (F) Atomic diagram of a hexagonal 2D α-Mo$_2$C crystal. Different colored atoms represent different positions in unit cell (bottom in F).
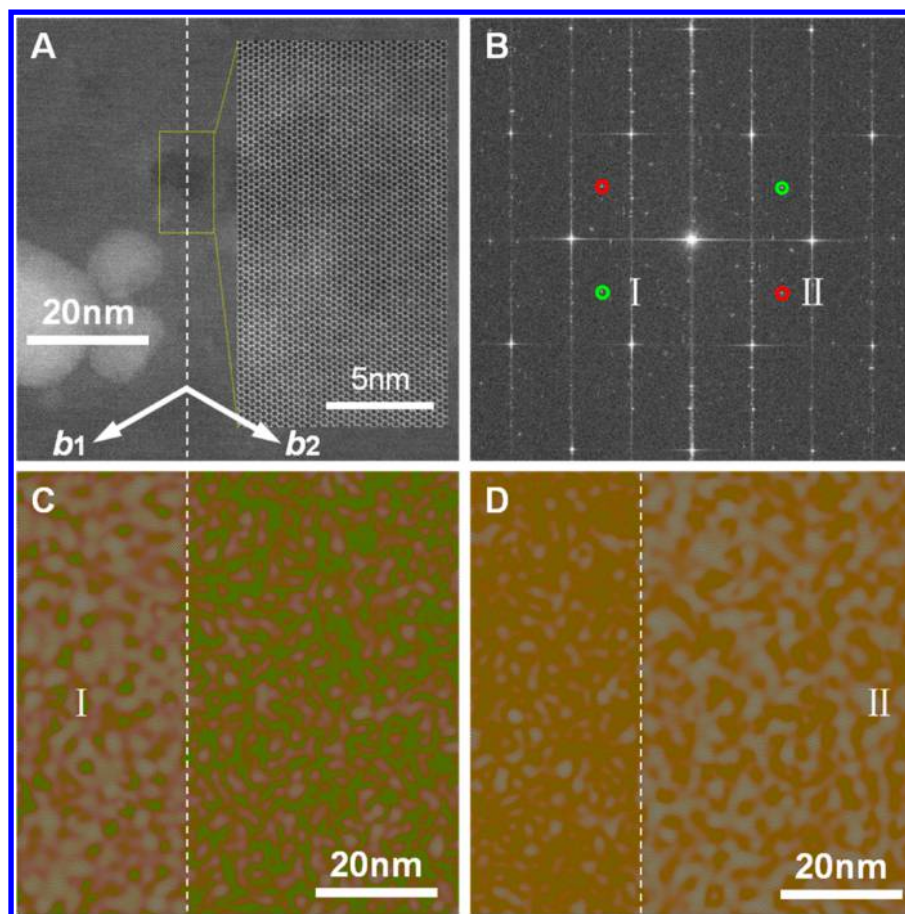
Figure 3. Sixty degree domain boundary in a 2D α-Mo$_2$C crystal. (A) HAADF-STEM image in the vicinity of the domain boundary. The white dashed line represents the position of the domain boundary, and the arrows show the lattice vector **b**-directions of each domain. A higher magnification HAADF-STEM image of the area indicated by the yellow dotted box shows that Mo atom sublattices connect seamlessly without defects across the domain boundary. (B) FFT of (A) showing two sets of (020) spots. (C,D) Inverse FFT images obtained from the type I spots indicated by the green circles (C) and type II spots indicated by the red circles (D) in B, clearly showing the domain boundary and the contrast difference between its two sides.

We also used SAED and DF-TEM to study the crystalline structure of α-Mo$_2$C crystals with other shapes. As shown in Figures S5−S7, triangular, nonagonal, and dodecagonal crystals are also multidomain superstructures, which are respectively composed of three triangular, three pentagonal, and six pentagonal domains with rotational-symmetry. In these superstructures, similar to hexagonal crystals, the slightly distorted HCP Mo atom sublattices remain in the same orientation across the whole sheet, while the off-center zigzag configurations of carbon atoms in the adjacent domains are rotated by 60° or 120°. However, in these superstructures the direction of the off-center carbon atoms in each domain is perpendicular to the outer edge of the domain, which is different from the hexagonal superstructure. In contrast, rectangular and octagonal crystals are single-domain crystals without domain boundaries (Figure S8). Moreover, it is worth noting that the characteristic of domain structure in all shaped crystals is independent of crystal thickness, as shown in Figure S9.

It is important to note from the above results that all the 2D α-Mo$_2$C superstructures are composed of very regular domains with 3-fold or 6-fold rotational-symmetry and well-defined line-shaped domain boundaries. This structure characteristic has not been observed before in any other 2D materials such as graphene and atomically thin transition metal dichalcogenides and even bulk TMC materials. It is well-known that the

morphology of a crystal is closely associated with its crystallographic symmetry. Similar to previously reported results,[22] CVD-grown 2D Mo$_2$C superstructures might undergo a phase transition from a high temperature hexagonal phase (β-Mo$_2$C) to a room temperature orthorhombic phase (α-Mo$_2$C). In this phase transition process, carbon atoms move from randomly occupying centers of octahedral interstices to an ordered occupation arrangement in positions slightly offset from the octahedron centers with zigzag configuration. The three equivalent zigzag configurations of carbon atoms in a 2D α-Mo$_2$C crystal can assemble to produce 6-fold rotational-symmetry. Therefore, for hexagonal 2D α-Mo$_2$C crystals, six triangular domains are formed with a pseudo-6-fold symmetry to maintain their original 6-fold crystallographic symmetry and harmonize the resulting strains between different domains. Based on symmetry considerations, triangular crystals can be regarded as a degeneration of the 6-fold symmetry of the high temperature hexagonal phase, and nonagonal and dodecagonal crystals can be respectively regarded as truncated triangular and hexagonal crystals. Therefore, all these shaped crystals are transited to orthorhombic phases containing domains with 3- or 6-fold symmetry during the phase transition process. In contrast, a rectangular 2D α-Mo$_2$C crystal and its truncated counterpart, an octagonal crystal, have mirror and 2-fold symmetry, which means that only one zigzag configuration of
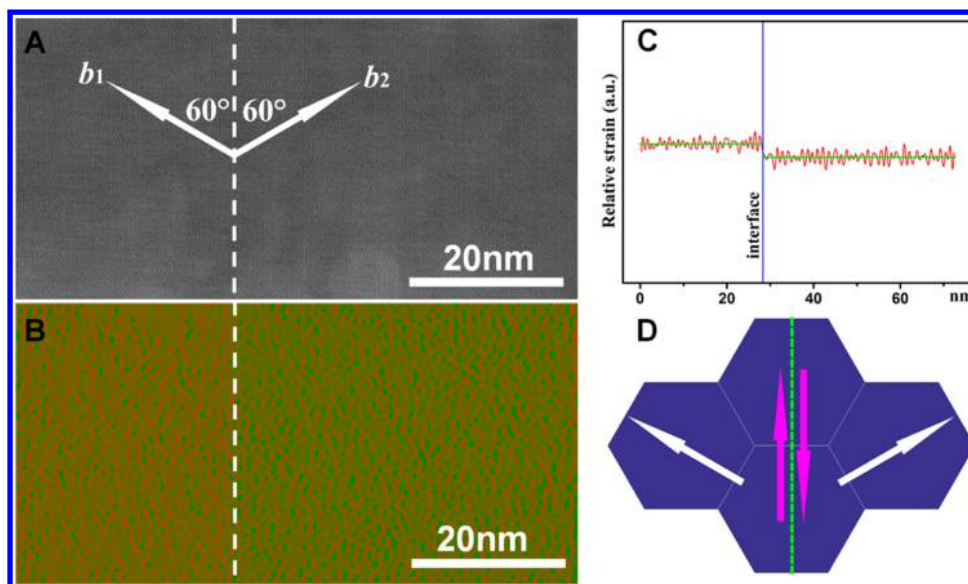
Figure 4. Relative lattice shear strain across a 60°-domain boundary. (A) HAADF-STEM image in the vicinity of a 60°-domain boundary. (B) Relative lattice shear strain map extracted from (A) based on GPA analysis. (C) Profile of average relative shear strain perpendicular to a domain boundary. (D) Schematic of the production of relative shear strain. The dark blue hexagons represent the projected Mo octahedra, the white arrows represent the off-center directions of the octahedral interstitial carbon atoms, and the pink arrows represent the relative shear strain direction.
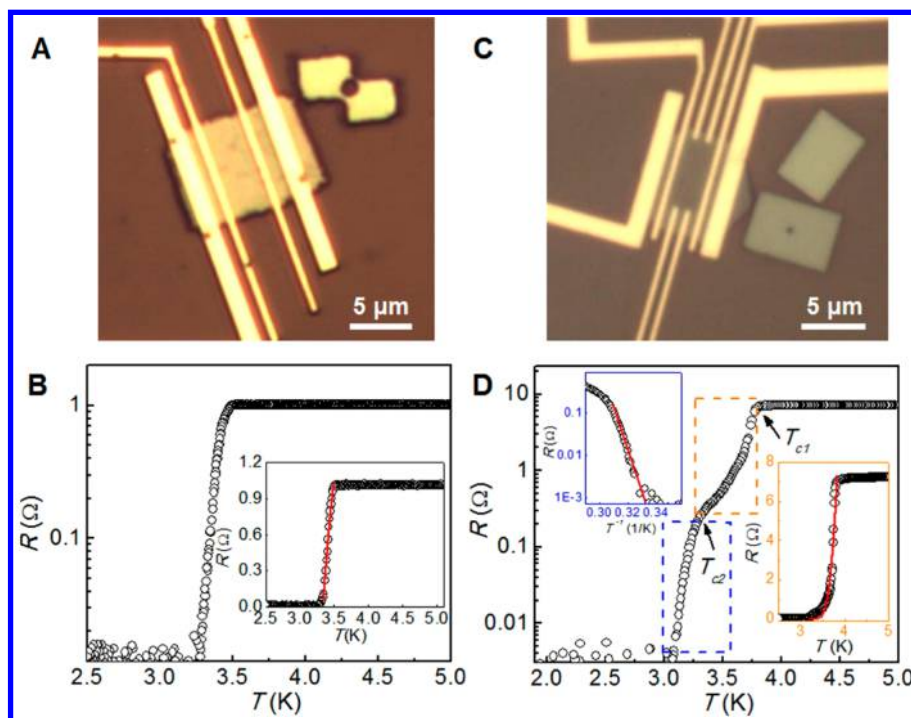
Figure 5. Influence of domain boundaries on the superconductivity of 2D α-Mo$_2$C superconductors. (A,B) Optical image (A) and the temperature-dependent resistive $R(T)$ superconducting transition (B) of a device made from a 7.6 nm-thick rectangular single-domain 2D α-Mo$_2$C crystal. The red solid line in the inset of B represents a fit to the $R(T)$ curve following the Halperin–Nelson formula based on the BKT model. (C,D) Optical image (C) and the temperature-dependent resistive superconducting transitions (D) of a device made from a 8.3 nm-thick hexagonal multidomain 2D α-Mo$_2$C crystal with 60°-domain boundary. Lower inset: The red solid line is a fit to the expected BKT transition for a single-phase 2D superconductor. Upper inset: Arrhenius plot of the measured resistance of a hexagonal crystal sample. The solid line is a linear fit to the data, showing thermally activated behavior in the lower superconducting transition regime.

carbon atoms is selected during the phase transition process, leading to the formation of single-domain crystals.

In terms of domain boundaries, all the domains with rotational-symmetry in different shaped α-Mo$_2$C superstructures have 60° or 30° angles between the octahedron off-center directions of carbon atoms and the domain boundary lines

(Figure S10). The corresponding boundaries are defined as 60°- and 30°-domain boundaries. To reveal the carbon and Mo atom arrangements at domain boundary, we performed atomic-resolution STEM experiments and theoretical calculations. Figures 3A and S11A show HAADF-STEM images in the vicinity of 60°- and 30°-domain boundaries, respectively. The

corresponding FFT patterns show two sets of domain related (020) type spots (Figures 3B and S11B), indicating different directions of the distortion of HCP Mo atom sublattices (lattice vector **b**-directions in Figures 3A and S11A) that are caused by the different off-center zigzag configurations of carbon atoms. The inverse FFT images obtained from different types of spots clearly show a sharp domain boundary (Figures 3C,D and S11C,D). It can be seen that the Mo atom sublattices connect seamlessly without any defects across the domain boundaries in both cases (Figures 3A and S11E). As mentioned above, even though the carbon atoms can be seen in BF-STEM images, we could not determine their spatial occupation information in the vicinity of the domain boundaries. Therefore, we constructed atomic models to simulate this. Based on the premise that the stoichiometric ratio of α-Mo$_2$C is unchanged at domain boundaries, there are two interfacial configurations of carbon atoms associated with both 60°- and 30°-domain boundaries, forming symmetric and asymmetric domain boundaries in both cases (Figure S12). Table S2 shows the calculated interfacial energies of these domain boundaries based on first-principles calculations. The symmetric domain boundaries are more stable than the asymmetric ones for both 60°- and 30°-domain boundaries, and we therefore suggest that all the α-Mo$_2$C superstructures may have symmetric domain boundaries because of this higher stability, as shown in Figure 2F.

As shown in Figures 3C,D and S11C,D, the HCP Mo atom sublattices in adjacent domains are distorted in different directions. Therefore, this is expected to produce a relative lattice shear strain across the domain boundary. Geometric phase analysis (GPA) is an effective method to extract the strain information in crystalline structures from HRTEM and HRSTEM images by analyzing reciprocal space vectors.[23,24] Figure 4A shows a HAADF-STEM image extracted from Figure 3A, and the dashed line shows the position of the domain boundary. Figure 4B shows the lattice shear strain map extracted from the HAADF-HRSTEM image in Figure 4A. It can be seen that the lattice shear strain is very uniform in each domain, further confirming the high structural uniformity of our 2D α-Mo$_2$C crystals. More importantly, the contrast difference of shear strain on the two sides of the boundary is very small, indicating a small relative shear strain across it. Nevertheless, we still could see the domain boundary based on contrast difference. We further extracted the average shear strain perpendicular to the domain boundary from Figure 4B. As shown in Figure 4C, the obtained profile clearly shows the relative shear strain across the domain boundary even though it is small. Figure 4D shows a schematic of the production of relative lattice shear strain at the 60°-domain boundary. The 30°-domain boundary also shows a quite small lattice shear strain across the domain boundary (Figure S13).

These high-quality 2D α-Mo$_2$C superconducting crystals with sharp domain boundaries provide an ideal platform to investigate the intrinsic influence of domain boundaries on 2D superconductivity (Figure 5). Figure 5A shows an optical image of a 7.6 nm-thick rectangular single-domain α-Mo$_2$C crystal device with a four-terminal configuration. The temperature-dependent resistance $R(T)$ of the device at zero magnetic field is shown in Figure 5B. A sharp drop of resistance, characteristic of the superconducting transition, is clearly observed below the critical temperature $T_c \approx 3.5$ K, indicating a uniformly defined superconducting state. Figure 5C shows the optical image of a device made from an 8.3 nm-thick hexagonal multidomain α-Mo$_2$C crystal with 60°-domain boundary, which allows the

measurement of electron transport across the domain boundary. In contrast to the single-domain rectangular α-Mo$_2$C crystal, the hexagonal crystal sample shows a broadened superconducting transition (Figure 5D). Moreover, it shows two distinct resistive superconducting transitions at $T_{c1} \approx 3.8$ K and $T_{c2} \approx 3.3$ K as marked in Figure 5D. As confirmed by atomic-resolution STEM observations, our 2D α-Mo$_2$C crystals have very high crystallinity without defects except for the domain boundaries. Therefore, our results give clear evidence that a domain boundary has a strong influence on 2D superconductivity. The resulting two-step resistive transitions are different from the multistep resistive transitions observed earlier in amorphous superconducting films and wires, which are attributed to an inhomogeneous superconducting phase or a phase separation in the superconducting state.[25,26]

To understand the resistive transitions in more detail, we have analyzed the measured $R(T)$ curves in terms of the theoretical models of the Berezinskii−Kosterlitz−Thouless (BKT) transition and thermally activated phase slip.[27−29] The red solid line in the inset of Figure 5B is a fit to the measured $R(T)$ curve of the rectangular single-domain crystal sample using the Halperin−Nelson equation:[28]

$$R = R_0 \exp(-bt^{-1/2}) \tag{1}$$

where R_0 and b are material-specific parameters, and $t = T/T_{BKT} - 1$ is the reduced temperature. The fitting result indicates that the superconducting transition in the single-domain crystal is consistent with expectations for a single-phase 2D superconductor based on the BKT model.[27] In the lower inset of Figure 5D, we present a fit to the measured $R(T)$ curve of a hexagonal multidomain crystal sample using eq 1, showing that the resistance drop in the higher temperature regime can be well described quantitatively by the BKT model, similar to the observations in single-domain crystals. As reported in our previous paper,[14] the higher critical transition temperature compared to that of rectangular single-domain crystal shown in Figure 5b is attributed to the larger thickness of the hexagonal crystal. However, there is a clear deviation from the BKT model as the temperature is lowered. In an Arrhenius plot of $R(T)$ as shown in the upper inset of Figure 5D, the temperature variation of resistance in the second transition can be modeled using thermally activated transport. As shown above, the domain boundaries in our crystals are very sharp, with a width of a few atoms, which is much smaller than the superconducting coherence length ($\sim$20 nm).[14] Therefore, they can be considered one-dimensional superconducting wires. For one-dimensional superconductors, a finite resistance arises due to thermally activated phase slip process. In this case, the resistance is given by the equation,[29,30] $R(T) \approx \exp(-\Delta F/k_B T)$, where ΔF is the free energy barrier for phase slip and k_B is the Boltzmann constant. It is worth noting that the fit to the thermally activated phase slip model (red solid line in the upper inset of Figure 5D) agrees well with the measured $R(T)$ data. Therefore, the observed two-step superconducting transition of $R(T)$ in multidomain crystals can be understood by a transition in a single-domain phase and localized phase slip events at the domain boundary.

It should be noted that all the measured hexagonal and other-shaped multidomain α-Mo$_2$C crystals show a broadened transition temperature width and two-step transitions. Figure S14 shows the $R(T)$ curve of a device made from a 6.9 nm-thick dodecagonal multidomain 2D α-Mo$_2$C crystal with 30°-domain boundary. Similar to the hexagonal crystal with 60°-

domain boundary, this curve also can be fit by a transition in a single-domain phase based on the BKT model (high temperature regime) and a domain boundary-related transition based on thermally activated phase slip model (low temperature regime). This indicates that the two-step superconducting transition is intrinsic to the presence of the domain boundaries in 2D α-Mo_2C superconductors. However, the measured $R(T)$ curve of the dodecagonal α-Mo_2C crystal exhibits more enhanced deviation from the BKT model for single-domain crystal than hexagonal sample as the temperature is lowered. Note that both the hexagonal and dodecagonal crystals contain six domain boundaries (Figures 2, S7, and S10). These results imply that the orientation of the domain boundary lines relative to the octahedron off-center directions of carbon atoms may have an influence on the superconducting transition behaviors of multidomain crystals, which requires further investigations both experimentally and theoretically in the future.

In summary, we have studied the crystalline structure of CVD grown 2D α-Mo_2C superconducting crystals of triangular, rectangular, hexagonal, octagonal, nonagonal, and dodecagonal shapes. For all shaped crystals, the Mo atom sublattice has uniform hexagonal closely packed arrangement across the crystal without any boundaries. However, except for rectangular and octagonal crystals, the C atom sublattices are composed of three or six domains with rotational-symmetry and well-defined line-shaped domain boundaries because of the presence of three equivalent octahedron off-center zigzag configurations of carbon atoms. We found that there is relatively small lattice shear strain across the the domain boundary, but the domain boundary has a significant influence on the superconductivity of 2D α-Mo_2C crystals because of the formation of localized phase slip events within the boundaries, leading to a broad resistive superconducting transition with two distinct transition processes rather than a single sharp transition observed in single-domain crystals. These findings provide new insights into not only the crystalline structure of 2D TMC crystals but also the intrinsic influence of domain boundary on 2D superconductivity.

ASSOCIATED CONTENT

Ⓢ Supporting Information

The Supporting Information is available free of charge on the ACS Publications website at DOI: 10.1021/acs.nanolett.6b01265.

Methods, characterizations, calculations, simulations, and measurements (PDF)

AUTHOR INFORMATION

Corresponding Authors
*E-mail: xlma@imr.ac.cn. Fax: 86-24-23891320.
*E-mail: wcren@imr.ac.cn. Fax: 86-24-23971682.

Author Contributions
Z.L., C.X., and N.K. contributed equally to this work. W.R. conceived and supervised the project; Z.L. performed TEM measurements and analyses under supervision of X.-L.M.; C.X. grew samples under supervision of W.R. and H.-M.C.; L.W. and J.D. carried out transport measurements under supervision of N.K.; Y.J. performed theoretical simulations; Y.L. helped with TEM measurements; W.R., Z.L., and N.K. analyzed data and wrote the manuscript. All the authors discussed the results and commented on the manuscript.

REFERENCES

(1) Novoselov, K. S.; Geim, A. K.; Morozov, S. V.; Jiang, D.; Zhang, Y.; Dubonos, S. V.; Grigorieva, I. V.; Firsov, A. A. *Science* **2004**, *306*, 666−669.
(2) Novoselov, K. S.; Jiang, D.; Schedin, F.; Booth, T. J.; Khotkevich, V. V.; Morozov, S. V.; Geim, A. K. *Proc. Natl. Acad. Sci. U. S. A.* **2005**, *102*, 10451−10453.
(3) Geim, A. K.; Grigorieva, I. V. *Nature* **2013**, *499*, 419−425.
(4) Wang, Q. H.; Kalantar-Zadeh, K.; Kis, A.; Coleman, J. N.; Strano, M. S. *Nat. Nanotechnol.* **2012**, *7*, 699−712.
(5) Huang, P. Y.; Ruiz-Vargas, C. S.; van der Zande, A. M.; Whitney, W. S.; Levendorf, M. P.; Kevek, J. W.; Garg, S.; Alden, J. S.; Hustedt, C. J.; Zhu, Y.; Park, J.; McEuen, P. L.; Muller, D. A. *Nature* **2011**, *469*, 389−392.
(6) Tsen, A. W.; Brown, L.; Levendorf, M. P.; Ghahari, F.; Huang, P. Y.; Havener, R. W.; Ruiz-Vargas, C. S.; Muller, D. A.; Kim, P.; Park, J. *Science* **2012**, *336*, 1143−1146.
(7) Lee, G. H.; Cooper, R. C.; An, S. J.; Lee, S.; van der Zande, A.; Petrone, N.; Hammerberg, A. G.; Lee, C.; Crawford, B.; Oliver, W.; Kysar, J. W.; Hone, J. *Science* **2013**, *340*, 1073−1076.
(8) van der Zande, A. M.; Huang, P. Y.; Chenet, D. A.; Berkelbach, T. C.; You, Y.; Lee, G. H.; Heinz, T. F.; Reichman, D. R.; Muller, D. A.; Hone, J. C. *Nat. Mater.* **2013**, *12*, 554−561.
(9) Yazyev, O. V.; Chen, Y. P. *Nat. Nanotechnol.* **2014**, *9*, 755−767.
(10) Li, X.; Cai, W. W.; An, J. H.; Kim, S.; Nah, J.; Yang, D. X.; Piner, R.; Velamakanni, A.; Jung, I.; Tutuc, E.; Banerjee, S. K.; Colombo, L.; Ruoff, R. S. *Science* **2009**, *324*, 1312−1314.
(11) Gao, Y.; Liu, Z.; Sun, D. M.; Huang, L.; Ma, L. P.; Yin, L. C.; Ma, T.; Zhang, Z.; Ma, X. L.; Peng, L. M.; Cheng, H. M.; Ren, W. *Nat. Commun.* **2015**, *6*, 8569.
(12) Lin, Y. H.; Nelson, J.; Goldman, A. M. *Phys. C* **2015**, *514*, 130−141.
(13) Cao, Y.; Mishchenko, A.; Yu, G. L.; Khestanova, E.; Rooney, A. P.; Prestat, E.; Kretinin, A. V.; Blake, P.; Shalom, M. B.; Woods, C.; Chapman, J.; Balakrishnan, G.; Grigorieva, I. V.; Novoselov, K. S.; Piot, B. A.; Potemski, M.; Watanabe, K.; Taniguchi, T.; Haigh, S. J.; Geim, A. K.; Gorbachev, R. V. *Nano Lett.* **2015**, *15*, 4914−4921.
(14) Xu, C.; Wang, L.; Liu, Z.; Chen, L.; Guo, J.; Kang, N.; Ma, X. L.; Cheng, H. M.; Ren, W. *Nat. Mater.* **2015**, *14*, 1135−1141.
(15) Naguib, M.; Mochalin, V. N.; Barsoum, M. W.; Gogotsi, Y. *Adv. Mater.* **2014**, *26*, 992−1005.
(16) Ghidiu, M.; Lukatskaya, M. R.; Zhao, M.; Gogotsi, Y.; Barsoum, M. W. *Nature* **2014**, *516*, 78−81.
(17) Lukatskaya, M. R.; Mashtalir, O.; Ren, C. E.; Dall'Agnese, Y.; Rozier, P.; Taberna, P. L.; Naguib, M.; Simon, P.; Barsoum, M. W.; Gogotsi, Y. *Science* **2013**, *341*, 1502−1505.
(18) Parthé, E.; Sadagopan, V. *Acta Crystallogr.* **1963**, *16*, 202−205.
(19) Tang, Y. L.; Zhu, Y. L.; Ma, X. L.; Borisevich, A. Y.; Morozovska, A. N.; Eliseev, E. A.; Wang, W. Y.; Wang, Y. J.; Xu, Y. B.; Zhang, Z. D.; Pennycook, S. J. *Science* **2015**, *348*, 547−551.
(20) Jia, C. L.; Urban, K. W.; Alexe, M.; Hesse, D.; Vrejoiu, I. *Science* **2011**, *331*, 1420−1423.
(21) Catalan, G.; Seidel, J.; Ramesh, R.; Scott, J. F. *Rev. Mod. Phys.* **2012**, *84*, 119−156.
(22) Christensen, A. N. *Acta Chem. Scand.* **1977**, *31*, 509−511.
(23) Hytch, M. J.; Snoeck, E.; Kilaas, R. *Ultramicroscopy* **1998**, *74*, 131−146.

(24) Hytch, M. J.; Putaux, J. L.; Thibault, J. *Philos. Mag.* **2006**, *86*, 4641−4656.

(25) Wang, H.; Rosario, M. M.; Kurz, N. A.; Rock, B. Y.; Tian, M.; Carrigan, P. T.; Liu, Y. *Phys. Rev. Lett.* **2005**, *95*, 197003.

(26) Parendo, K. A.; Tan, K. H. S. B.; Goldman, A. M. *Phys. Rev. B: Condens. Matter Mater. Phys.* **2007**, *76*, 100508.

(27) Berezinskii, V. L. *Sov. Phys. JETP* **1972**, *34*, 610−616.

(28) Halperin, B. I.; Nelson, D. R. *J. Low Temp. Phys.* **1979**, *36*, 599−616.

(29) Langer, J. S.; Ambegaokar, V. *Phys. Rev.* **1967**, *164*, 498.

(30) Arutyunov, K. Y.; Golubev, D. S.; Zaikin, A. D. *Phys. Rep.* **2008**, *464*, 1−70.